



# Optoelectronic and structural properties of multilayer oxide/silver/oxide transparent conducting electrodes using green laser annealing

Manikandan Rajendran<sup>1</sup> · Keh-Moh Lin<sup>1</sup>

Received: 13 March 2024 / Revised: 18 April 2024 / Accepted: 22 April 2024 / Published online: 6 May 2024  
© The Korean Physical Society 2024

## Abstract

Transparent conducting ITO/Ag/ITO (IAI) and AZO/Ag/AZO (ZAZ) multilayer electrodes were fabricated using radio frequency magnetron sputtering at room temperature. Subsequently, a green laser was employed for annealing these multilayer films to improve their optical, electrical, and structural properties. Their optical and electrical properties were characterized using a UV–Vis spectrophotometer, and a four-point probe station, respectively, while structural properties were characterized using X-ray diffraction (XRD) and transmission electron microscopy (TEM). After laser annealing, XRD analysis indicated an increase in Ag intensity peak, correlating with larger crystallite size post-annealing. TEM analysis confirmed the formation of a continuous structure as weakly connected Ag crystallites bonded during the annealing process. The IAI electrodes showed significant improvement, reducing sheet resistance from 8.2  $\Omega/\text{sq}$  to 6.9  $\Omega/\text{sq}$ , and the Haacke index improved from  $\phi_{\text{vis}} \approx 17 \times 10^{-3} \Omega^{-1}$  to  $\phi_{\text{vis}} \approx 21 \times 10^{-3} \Omega^{-1}$ . In contrast, the physical properties of the ZAZ electrodes could not be further improved by the laser annealing process, as their Ag layers already exhibited high crystallinity. Our results indicate that optimizing the conductivity of the Ag layer is crucial for the optoelectronic performance of multilayer electrodes. This optimization can be achieved through laser annealing with suitable energy densities and using oxide layers promoting dense Ag growth.

**Keywords** Transparent conducting electrode · Laser annealing · Sputtering · Silver layer · Microstructure · Optoelectronic properties

## 1 Introduction

Transparent conducting oxides (TCOs) play a crucial role in optoelectronic devices, and it is widely employed as a current conducting layer in various optoelectronic devices such as photovoltaic solar cells [1], organic light-emitting diodes [2], liquid crystal displays [3], flat panel displays [4], touch panels [5], and smart windows [6]. Among TCOs, indium tin oxide (ITO) is extensively used in the optoelectronic industries due to its low sheet resistance and high optical transmittance, surpassing alternatives like  $\text{SnO}_2$ , ZnO, and fluorine-doped tin oxide (FTO) electrodes [7–10]. Various deposition techniques are involved in fabricating TCO electrodes, such as sol–gel [11], thermal evaporation

[12], e-beam evaporation [13], spray pyrolysis [14], pulsed laser deposition [15], chemical vapor deposition [16], direct current (DC) sputtering [17], and radio frequency (RF) sputtering [18]. Among these methods, RF sputtering is widely adopted for its ability to deposit large substrate areas while ensuring superior film quality and robust adhesion [19, 20]. While ITO remains a leading candidate for transparent conducting electrodes, the growing demands of large-scale optoelectronic industries necessitate improvements in its physical characteristics. Increasing ITO thickness enhances electrical conductivity but the optical transmittance decreases, reducing the thickness of the ITO layer below 150 nm to achieve high-quality films with very low sheet resistance is quite challenging [21, 22].

Researchers recently proposed a multilayer structure (oxide/metal/oxide) for transparent conducting electrodes, offering benefits such as very low sheet resistance and high optical transmittance in the visible wavelength region [23–25]. In general, a thin metal layer, such as Ag, Cu, Au, or Ni, can be embedded between oxide layers to enhance

✉ Keh-Moh Lin  
kemo@stust.edu.tw

<sup>1</sup> Department of Mechanical Engineering, Southern Taiwan University of Science and Technology, Tainan 71005, Taiwan

electrical conductivity [26–31]. Among these, Ag stands out for its low absorption coefficient, high transparency, and superior conductivity [7, 32, 33]. Furthermore, the multilayer structure not only reduces the sheet resistance but also makes the device more cost-effective due to the lower consumption of ITO material [26, 27]. Consequently, the multilayer structure stands as a viable alternative to expensive ITO films.

Heating during film deposition or post-deposition annealing ( $> 300$  °C) is essential to enhance crystalline quality, reduce defects, and improve electrical conductivity and optical transmittance, resulting in more transparent films [27, 34]. However, traditional annealing methods risk surface and substrate damage due to prolonged high-temperature processes [35–38]. In addressing these challenges, laser annealing emerges as a promising alternative. The intense laser energy used in this method significantly reduces process time [39]. Several studies have employed different lasers for annealing transparent conducting electrodes. Kim et al. [40] explored the impact of excimer-laser annealing on sol-gel-derived ITO films, noting enhanced electrical properties, reduced resistivity, increased carrier density, and improved mobility with energy densities reaching up to  $240 \text{ mJ/cm}^2$ . W. Chung et al. [41] utilized XeCl excimer laser annealing to improve room temperature-deposited ITO films, reducing sheet resistance from  $191 \text{ } \Omega/\text{sq}$  to  $25 \text{ } \Omega/\text{sq}$  and increasing optical transmittance from 70% to over 85%. This study underscores the effectiveness of excimer laser annealing in optimizing thin film properties for diverse technological applications. Ding et al. [42] employed a UV laser for room temperature annealing of ZnO:Al (AZO) thin films, observing increased crystallinity and surface roughness with higher laser fluence, while thickness and elemental concentration remained minimally affected. G. Jo et al. [43] compared the effects of  $\text{CO}_2$  laser and RTA on Al-doped ZnO multilayer thin films, finding that  $\text{CO}_2$  laser significantly reduced sheet resistance, improving the figure of merit over 63 times compared to RTA. This study emphasizes the efficacy of RTA/ $\text{CO}_2$  laser annealing in enhancing the electrical and structural properties of ZnO-based thin films. In our previous study [44], a 355 nm UV laser was used to anneal ITO/Ag/ITO (IAI) multilayer electrodes, resulting in a polycrystalline structure with increased Ag crystallite size. The annealed electrodes exhibited high optical transmittance (85%) and low electrical resistivity ( $5.35 \text{ } \Omega/\text{sq}$ ). The Haacke index also increased from  $18.14 \times 10^{-3} \text{ } \Omega^{-1}$  to  $37.74 \times 10^{-3} \text{ } \Omega^{-1}$ , indicating improved crystalline quality after laser annealing.

As mentioned earlier, various studies have employed different lasers to anneal transparent conductive electrodes, showing enhancements in electrical and structural properties. However, the underlying mechanisms through which laser annealing affects the performance of multilayer

electrodes remain unexplored. In this investigation, we introduce the application of a green laser for annealing IAI and ZAZ multilayer electrodes, marking a contribution to the field of optoelectronics. We explore the effects of different laser spot sizes, specifically  $300 \text{ } \mu\text{m}$  (referred to as condition A),  $0.5 \text{ mm}$  (referred to as condition B), and  $1 \text{ mm}$  (referred to as condition C), on annealing IAI films. Additionally, laser spot sizes of  $0.5 \text{ mm}$  and  $1 \text{ mm}$  are applied to anneal ZAZ films. Subsequently, we conduct a comparative analysis of the optical, electrical, and structural properties of the IAI and ZAZ electrodes to elucidate the impact of the laser annealing process on the physical characteristics of these electrodes.

## 2 Experimental details

### 2.1 Fabrication of IAI and ZAZ electrodes

In this experimental investigation, a substrate composed of Corning® glass was employed as a substrate material, before deposition, the substrates underwent a thorough cleaning using acetone, followed by a subsequent treatment with alcohol, and ultimately rinsed with deionized water. This sequential cleaning methodology was implemented within an ultrasonic bath, aiming to eliminate impurities and surface contaminants. The glass substrates were subjected to a drying process utilizing nitrogen (purity 99.99%) gas to remove any residual moisture on the substrate surface. Subsequently, the fabrication of multilayer electrodes, specifically IAI and ZAZ, was achieved through RF magnetron sputtering. This deposition technique was conducted under ambient conditions. The high-purity targets used in the sputtering process included ITO, AZO, and Ag, each boasting a purity level of 99.9%. The experimental conditions included an 8 mtorr working pressure, a 5 cm target-to-substrate distance, and the argon gas with a purity level of 99.99% was used as a sputtering gas and the argon gas flow rate was 40 sccm. The ITO and AZO targets were subjected to 90 W of sputtering power, while the Ag target received 40 W. To improve the uniformity of the multilayered film, the sample holder was rotated at a speed of 5 rpm. The thickness of the intermediate Ag layer was maintained at 10 nm due to its high optical transmittance and very low sheet resistance. The optimum thickness was obtained in our previous experiment [25]. The top and bottom oxide layer's thickness was maintained at approximately 40 nm. In addition, before conducting our actual experiments, the ITO, AZO, and Ag targets were pre-sputtered in the Ar atmosphere to clean the target surface.

## 2.2 Laser annealing process

In this study, we utilized a diode-pumped solid-state 532 nm green laser system (532-10-V NANIO Industrial DPSS Laser) for the laser annealing process on the target sample surface. The green laser was operated in ambient air with fixed parameters: a laser power of 1.15 W, pulse repetition frequency set at 20 kHz, pulse width of 30 ns, line spacing of 0.05 mm, scanning speed of 500 mm/s, and scanning type configured as parallel lines. To introduce experimental variations, we adjusted the laser spot sizes to 300  $\mu\text{m}$ , 0.5 mm, and 1 mm during the experiments, aiming to achieve favorable induced optoelectronic properties in the samples.

## 2.3 Characterization

In this experimental configuration, we utilized analytical tools to comprehensively characterize the transparent conducting multilayer electrodes. An UV–Vis–NIR (Jacos V-670) spectrophotometer was employed for precise measurements of optical transmittance in the wavelength ranging from 300 nm to 1100 nm. Simultaneously, the four-point probe station (Keithley 2420) facilitated the accurate determination of sheet resistance. The thicknesses of the multilayer IAI and ZAZ electrodes were determined using a variable-angle spectroscopic ellipsometer (Wollam M-2000U). Thin-film X-ray diffractometry (Rigaku D/MAX 2500) with Cu  $K\alpha$  radiation ( $\lambda = 0.15406$  nm) was employed to

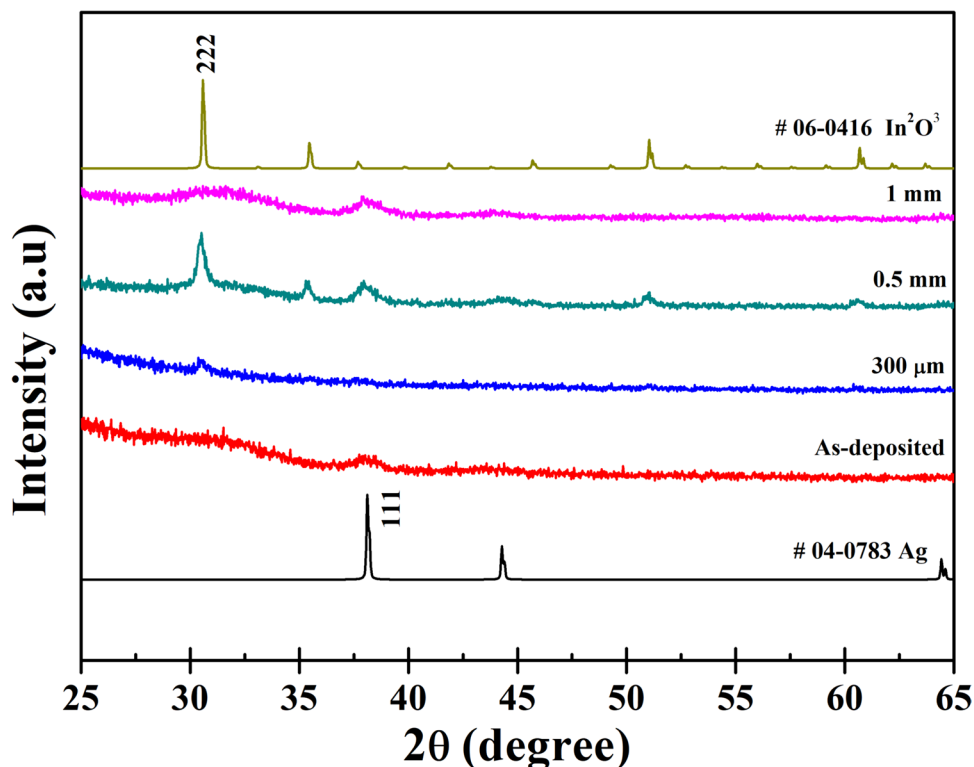
examine the crystal structures of the samples. Additionally, Transmission Electron Microscopy (JEOL-JEM 2010F) was employed to analyze the microstructure of the multilayer electrodes.

## 3 Results and discussion

### 3.1 ITO/Ag/ITO electrodes

Figure 1 shows the XRD patterns of both as-deposited and annealed IAI films. In the as-deposited film, the absence of the diffraction peak from the ITO film indicates its amorphous structure. However, a minor Ag diffraction peak is evident around  $38^\circ$  ( $2\theta$ ), corresponding to the (111)-plane [7]. After the laser annealing process, the sample under condition A showed signs of damage, and no ITO and Ag diffraction peaks were observed. In contrast, the sample under condition B displays robust ITO diffraction peaks with a cubic bixbyite structure, corresponding to the (222)-plane [41], and the Ag diffraction peak slightly increased, appearing around  $38^\circ$ , indicating a polycrystalline structure. In contrast, the sample under condition C shows no ITO diffraction peak, possibly due to the lower laser energy density. However, the Ag diffraction peak slightly increased. To assess the structural quality of the annealed film, crystallite sizes were estimated using the Scherrer equation [45].

**Fig. 1** XRD spectra of as-deposited and annealed films under conditions A, B, and C



$$D = \frac{K\lambda}{\beta \cos\theta}, \quad (1)$$

where  $D$  is the average crystallite size,  $K$  is the Scherrer constant ( $K=0.9$ ),  $\lambda$  is the X-ray wavelength ( $\lambda=1.5406 \text{ \AA}$ ),  $\beta$  is the full width half maximum (FWHM) of the diffraction peak, and  $\theta$  is the diffraction angle. The crystallite size increased from 7.1 nm to 10.6 nm for condition B and from 7.8 nm to 8.3 nm for condition C. A smaller laser spot size results in a higher heating energy density during the laser annealing process, leading to improved crystalline quality of the multilayer film. However, the very small laser spot size of 300  $\mu\text{m}$  resulted in excessive energy density during the annealing process, causing damage to the film.

Figure 2 illustrates the transmittance spectra of both as-deposited and annealed IAI films. The as-deposited film exhibits a notable transmittance value of 85% at a wavelength of 550 nm. The observed decrease in optical transmittance with increasing wavelength is attributed to the rise in

free electron concentration and interference effects within the multilayer structure [46, 47]. In Fig. 2a, the transmittance spectra of the sample under condition A indicate that this film was damaged. The transmittance spectra in Fig. 2b and c show that the optical transmittance in the visible wavelength region remained similar for the samples under condition B and condition C.

Figure 3a shows the average transmittance of as-deposited and annealed IAI films. The sample under condition B illustrated that its average transmittance in the visible region slightly decreased because of light scattering at the Ag Island structure [46]. However, a slight enhancement of average transmittance in the visible region was achieved for condition C, attributed to an increase in the crystalline quality of the films. In this case, it provided sufficient energy to connect weakly connected grains, forming a continuous film. To confirm the effectiveness of condition C, we conducted a verification experiment, as shown in Fig. 3b. The average transmittance of all samples was increased with an average

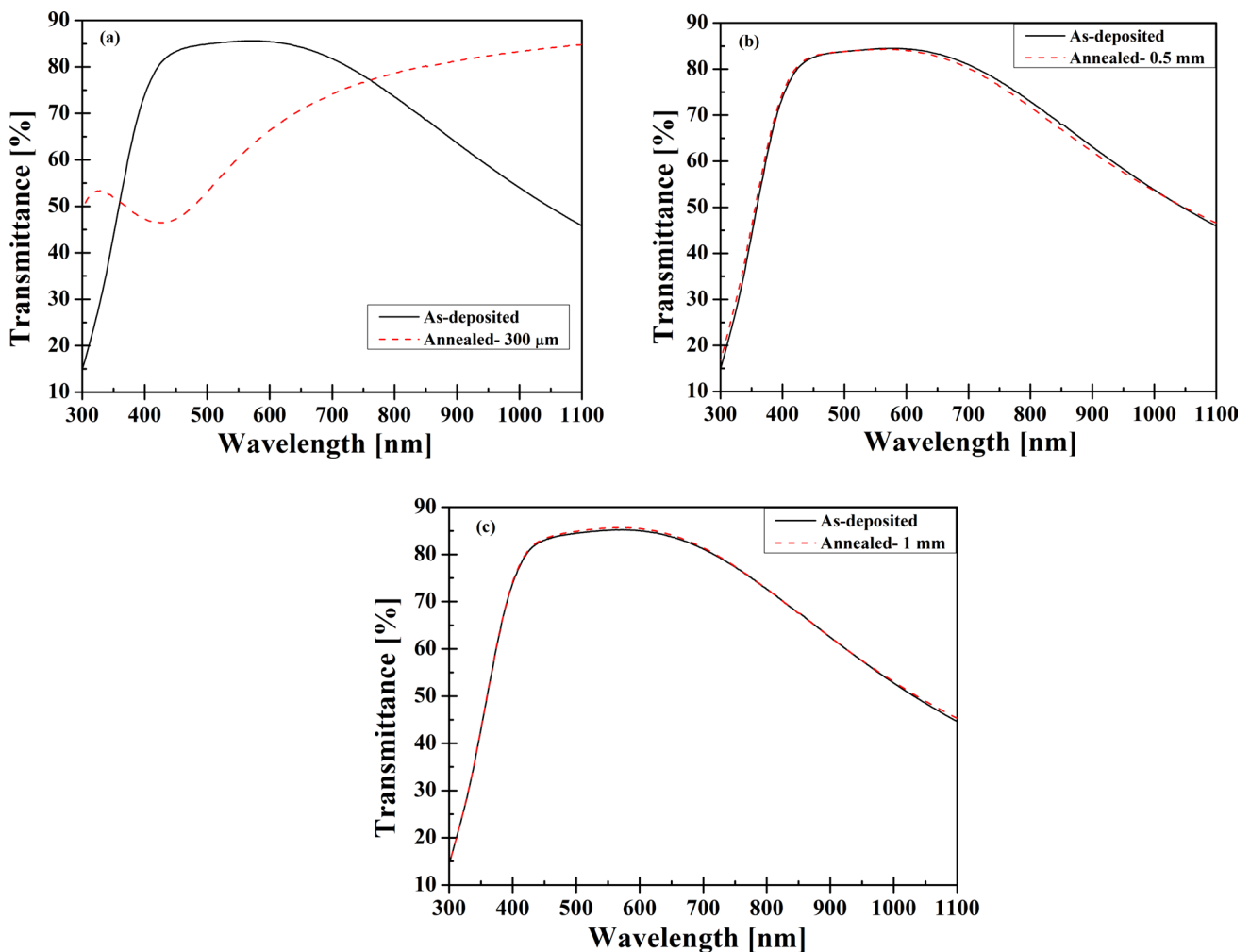


Fig. 2 Transmittance spectra of as-deposited and annealed films under **a** condition A, **b** condition B, and **c** condition C

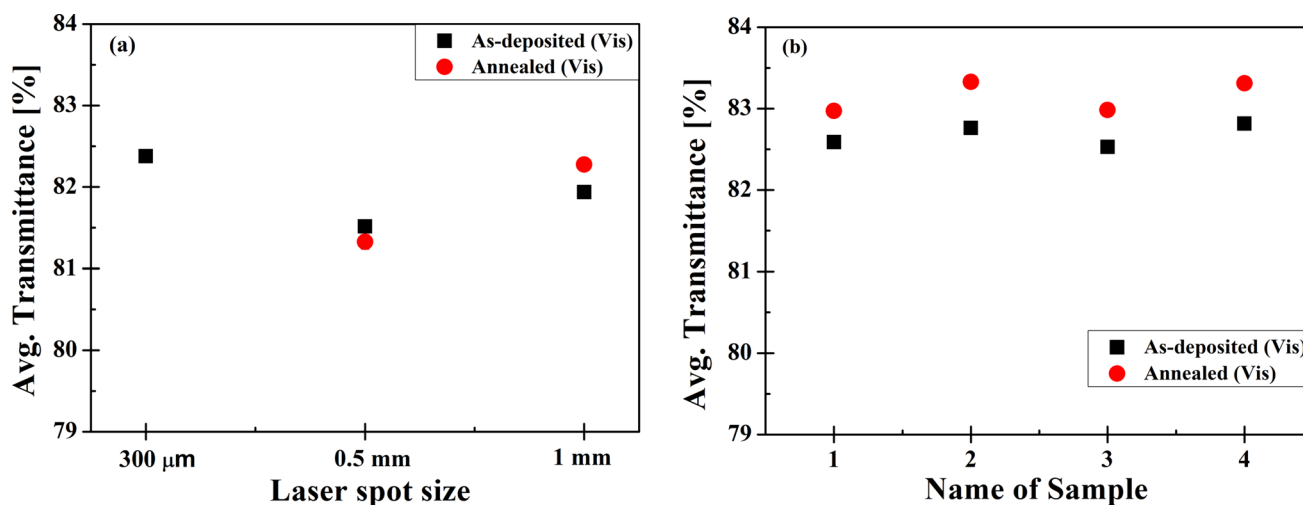


Fig. 3 a Avg. transmittance of as-deposited and annealed films under conditions A, B, and C, and b verification samples under condition C

transmittance of 83% in the visible region. This observation underscores the efficacy of condition C as a critical factor influencing the optical performance of the investigated samples.

Figure 4a shows the sheet resistance of as-deposited and annealed IAI films. The sample under condition B shows that the sheet resistance increased from 8.6 Ω/sq to 9.8 Ω/sq. This is due to the recrystallization of Ag crystallites to form disconnected islands during the annealing process. However, the sample under condition C illustrates that the sheet resistance significantly decreased from 8.2 Ω/sq to 6.9 Ω/sq due to the reduction of the defect density of the Ag film. In this case, a suitable energy flux went through the Ag film; therefore, the internal defects decreased, and the crystallite size slightly increased, as shown in the XRD spectra. The

crystallinity increased, thus the sheet resistance decreased dramatically. In the verification experiment illustrated in Fig. 4b, it was shown that the sheet resistance of all samples was significantly reduced.

Figure 5a illustrates the cross-sectional TEM image of the as-deposited IAI film. The top and bottom ITO layers exhibited the amorphous nature of the deposited film. The presence of the Ag layer between the top and bottom ITO layers was evident; however, the structure of weakly connected Ag islands between the ITO layers is noticeable. Figure 5b shows the cross-sectional TEM image of the IAI film annealed under condition C. The multilayer structure can be clearly identified. Both the top and bottom ITO layers were very smooth, indicating a nanocrystalline structure. The Ag layer between the top and bottom ITO layers exhibited a

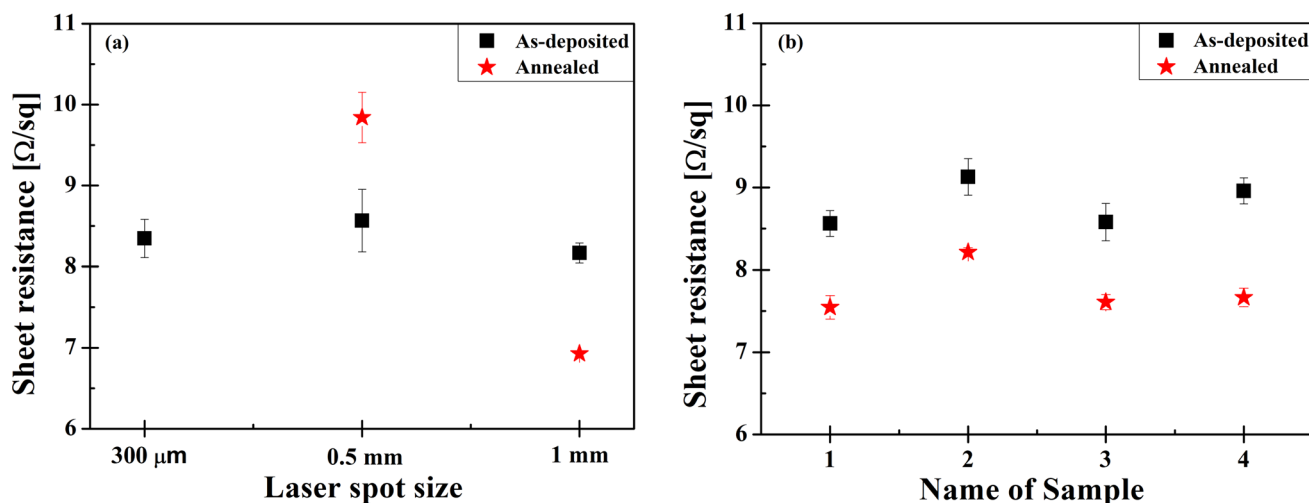
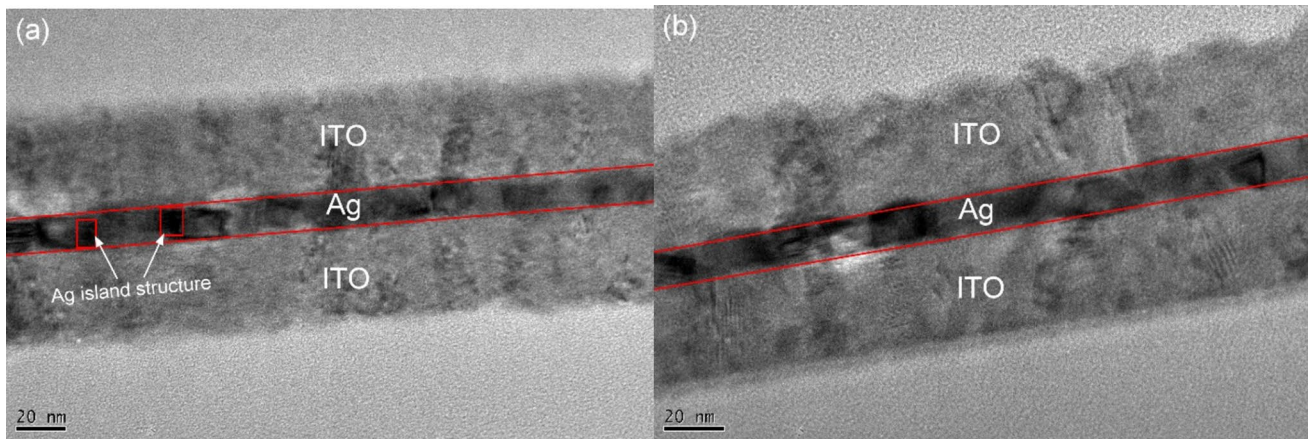


Fig. 4 a Sheet resistance of as-deposited and annealed films under conditions A, B, and C, and b verification samples under condition C



**Fig. 5** Cross-sectional TEM image of **a** as-deposited film and **b** annealed film under condition C

very smooth and continuous structure, indicating a lower defect density of the Ag film. The reduced number of defects contributed to a more uniform internal structure, effectively suppressing incident light scattering and improving carrier transport. Consequently, the overall structural quality is enhanced. Our XRD results also confirmed a slight increase in the intensity peak of Ag after laser annealing.

The evaluation of the transparent conducting multilayer electrodes was conducted through the Haacke index ( $\phi$ ) as a key performance metric [48]. The Haacke index is calculated using the below formula.

$$\phi = \frac{T^{10}}{R_s}, \quad (2)$$

where  $T$  is the average transmittance and the  $R_s$  corresponds to sheet resistance. A greater Haacke index value signifies

an improved balance between transmittance and sheet resistance. Figure 6a shows the Haacke index of the as-deposited and annealed films. The Haacke index of the samples from condition B decreased in the photovoltaic and visible regions. This was attributed to the reduced optical transmittance and increased sheet resistance. However, the Haacke index of the samples from condition C increased in the visible and photovoltaic regions. The increase in the Haacke index was mainly attributed to a decrease in sheet resistance. In the verification experiment under condition C, as illustrated in Fig. 6b, the Haacke index of all samples increased significantly. The highest Haacke index improvement, from  $\phi_{\text{Vis}} \approx 17 \times 10^{-3} \Omega^{-1}$  to  $\phi_{\text{Vis}} \approx 21 \times 10^{-3} \Omega^{-1}$ , was achieved. The results suggest that the green laser annealing process with a 1 mm laser spot size could effectively enhance the physical properties of IAI films.

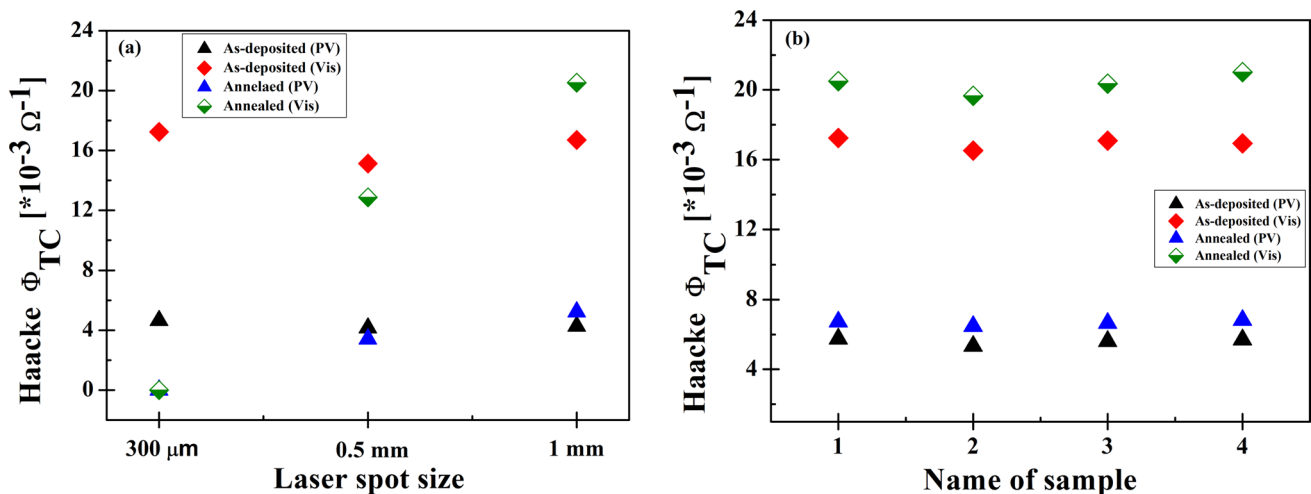


**Fig. 6** **a** Haacke index of the as-deposited and annealed films under conditions A, B, and C, and **b** verification samples under condition C

### 3.2 AZO/Ag/AZO electrodes

Figure 7 illustrates the XRD patterns of as-deposited and annealed ZAZ films. These XRD patterns reveal prominent peaks corresponding to the (002) and (111) planes of ZnO and Ag, respectively. To analyse the structural properties of the ZAZ films, we estimated the crystallite size using Scherrer's equation. The as-deposited Ag crystallite size was 11.7 nm, notably higher than the as-deposited Ag crystallite size of 6.2 nm–7.8 nm in the IAI films. Our findings suggest

that the structure of ZnO crystalline benefited the growth of Ag crystalline. The Ag crystallite sizes of ZAZ films under conditions B and C were 16.4 nm and 11.7 nm, respectively. No significant change in the crystallite size was observed under condition C. This indicates that the energy density under condition C did not induce the recrystallization process of the Ag layer.

Figure 8 shows transmittance spectra of as-deposited and annealed ZAZ films under condition B and C. The as-deposited film exhibited a remarkable transmittance of 87%

Fig. 7 XRD spectra of as-deposited and annealed films from conditions B and C

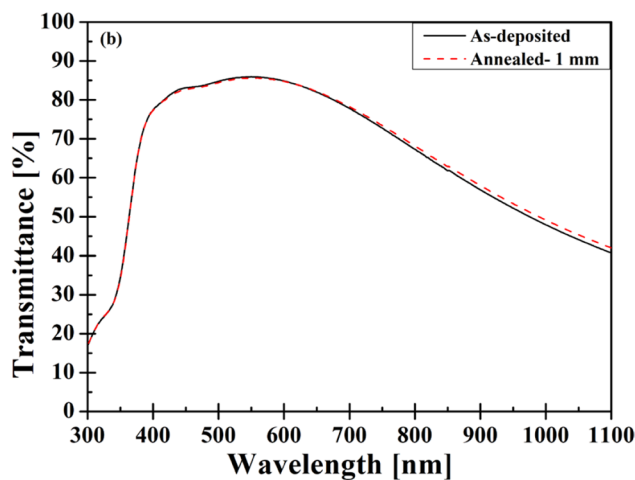
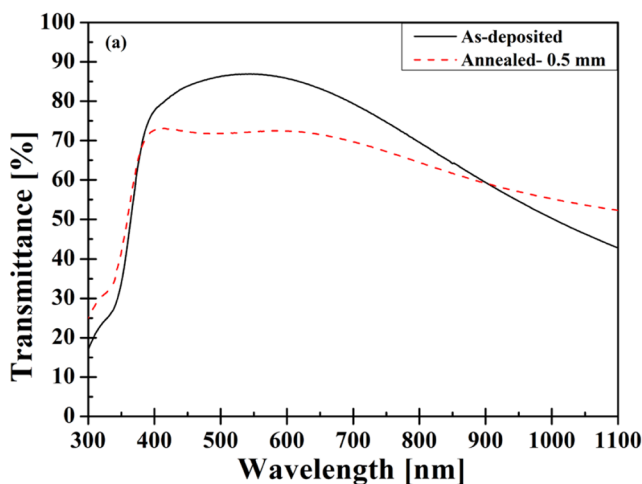
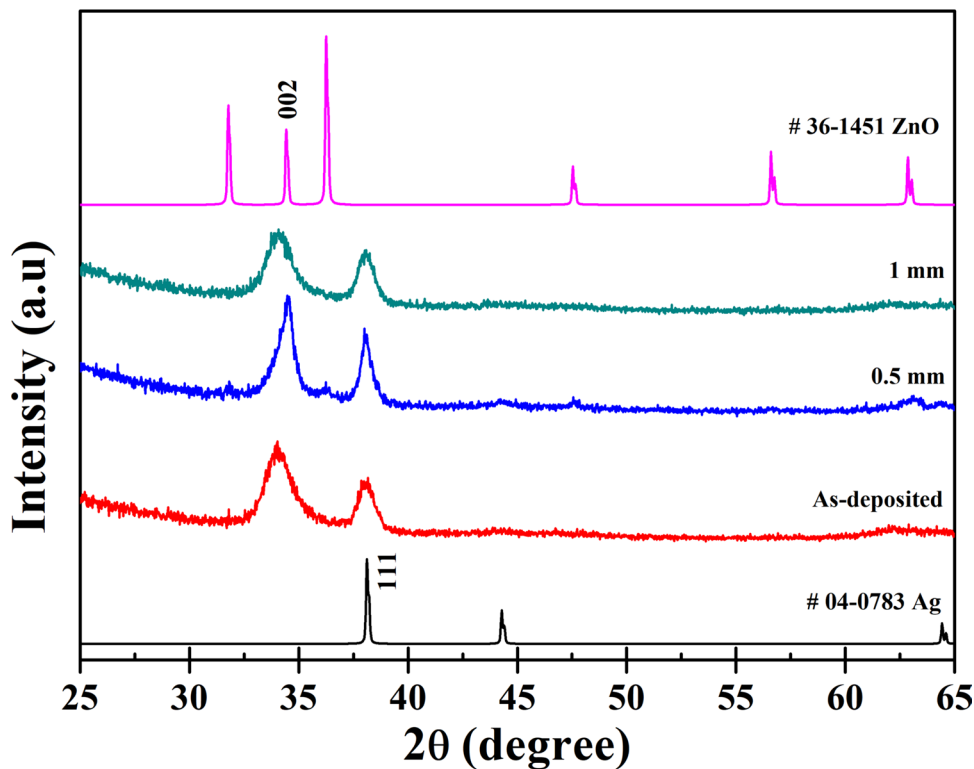


Fig. 8 Transmittance spectra of as-deposited and annealed ZAZ films under a condition B, and b condition C

at a wavelength of 550 nm. The increased transmittance in the visible region is attributed to the fact that the top and bottom AZO layers strongly act as anti-reflective layers, reducing incident light reflection from the intermediate Ag layer and increasing transmittance in the visible region [49]. The transmittance of the sample under condition B in Fig. 8a slightly increased in the UV and NIR regions, while it decreased noticeably in the visible region. The decrease in optical transmittance within the visible wavelength region is attributed to the uneven surface of the intermediate Ag layer after laser annealing. The higher energy density resulted in the formation of discontinuous Ag structures, leading to the creation of sizable Ag islands and a significant decline in optical transmittance. The transmittance of the sample under condition C in Fig. 8b remained constant in the UV, visible, and NIR regions. These findings suggest that condition C had no discernible effect on the transmittance spectrum of the ZAZ electrode.

In Fig. 9a and b, the average transmittance and sheet resistance of both as-deposited and annealed ZAZ films are presented. Condition B led to a significant drop in average transmittance, attributed to the recrystallization of the Ag film and the formation of discontinuous large Ag islands. The presence of these islands caused substantial light scattering, resulting in reduced average transmittance and increased sheet resistance due to the film structure's discontinuity. Moreover, the sample under condition C exhibited no noteworthy alterations in both average transmittance and sheet resistance. It indicates that the heating energy density under condition C did not provide enough driving force to modify the physical properties of Ag film in ZAZ electrodes. Furthermore, the crystallite sizes of as-deposited Ag films in ZAZ electrodes were larger than those in IAI electrodes, and the sheet resistance was also lower. These findings suggest

that the AZO layer promotes the deposition of a dense, highly conductive Ag layer, enhancing the optoelectronic properties of ZAZ electrodes.

Figure 10 illustrates the Haacke index of as-deposited and annealed film. As expected, the sample under condition B exhibited a low Haacke index in the visible region and photovoltaic region due to reduced optical transmittance and electrical conductivity. Additionally, sample condition C demonstrated a comparable Haacke index. These findings indicate that, under these conditions, the laser annealing process had minimal impact on the ZAZ films. The laser annealing did not improve ZAZ electrodes due to their already high crystallinity. Figure 11a and b illustrate the cross-sectional TEM images of both the as-deposited and annealed ZAZ films. These images confirmed the presence of a crystalline structure in both the as-deposited and annealed multilayer ZAZ films. Moreover, a slight diffusion of Ag into the AZO layer was observed, due to the heat induced by the laser during annealing. However, the increased crystalline quality observed in the as-deposited film could potentially lead to enhanced physical properties. The superior properties observed in the as-deposited ZAZ film suggest its suitability for various optoelectronic applications.

## 4 Conclusion

In this study, we investigated the structural, optical, and electrical properties of transparent conducting IAI and ZAZ electrodes prepared using RF magnetron sputtering. The multilayer films underwent green laser annealing with various laser spot sizes of 300  $\mu\text{m}$ , 0.5 mm, and 1 mm. Among these, the IAI films subjected to laser annealing under condition C demonstrated the highest average transmittance of

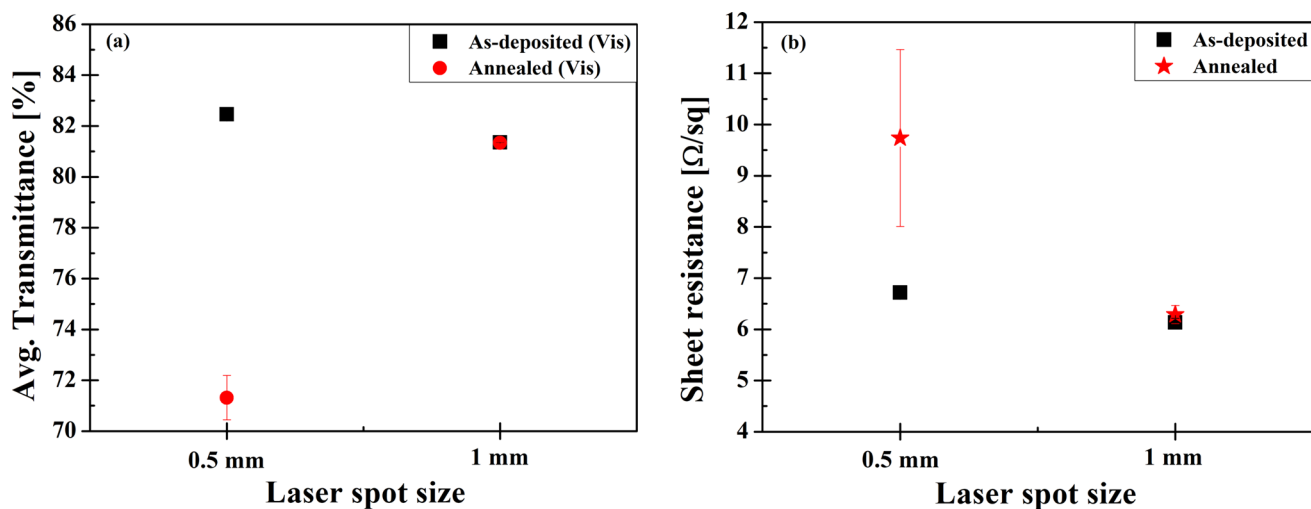
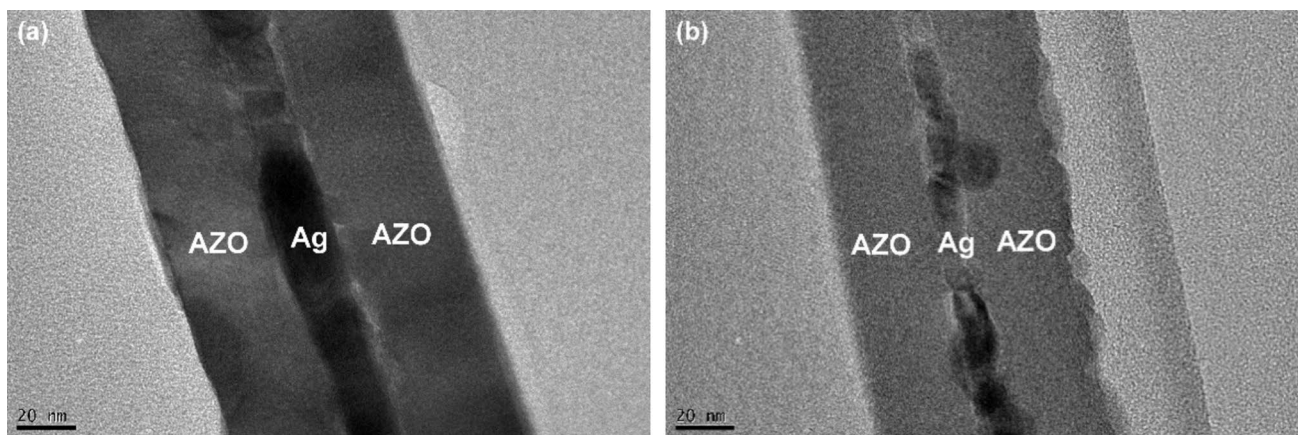
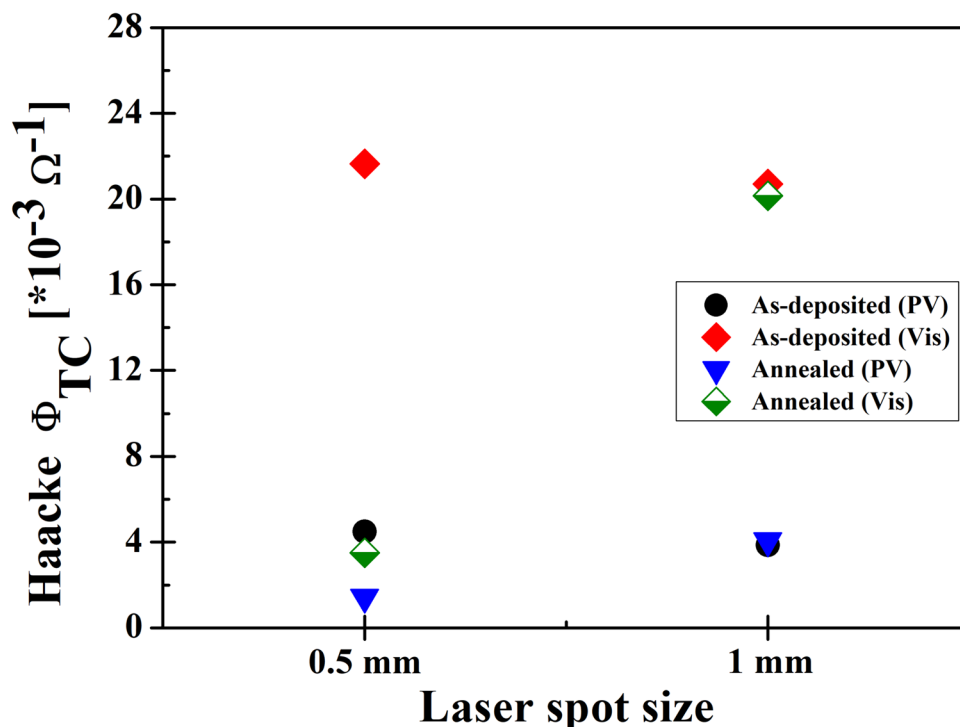


Fig. 9 a Avg. transmittance, b sheet resistance of as-deposited and annealed ZAZ films under conditions B and C



**Fig. 10** Haacke index of as-deposited and annealed ZAZ films under conditions B and C



**Fig. 11** Cross-sectional TEM image of **a** as-deposited film and **b** annealed ZAZ film under condition C

83% in the visible region. Concurrently, the sheet resistance experienced a significant reduction from 8.2  $\Omega/\text{sq}$  to 6.9  $\Omega/\text{sq}$ . Analysis of XRD results indicated an increase in the crystallite size of the Ag films after laser annealing. TEM analysis further identified that the Ag layer exhibits a very smooth and continuous structure after laser annealing. We comprehensively understand that the defect density of Ag films was reduced and crystalline quality increased during the annealing process. Additionally, The Haacke index significantly improved from  $\phi_{\text{Vis}} \cong 17 \times 10^{-3} \Omega^{-1}$  to  $\phi_{\text{Vis}} \cong 21 \times 10^{-3} \Omega^{-1}$ . In contrast, the ZAZ samples showed no improvements after laser annealing. This could be attributed

to the AZO layer being beneficial for depositing a dense and highly conductive silver layer, and the applied laser energy density may not significantly reduce the defect density of the Ag layer. Our results suggest that the conductivity of the Ag layer is a crucial factor in determining the optoelectronic performance of multilayer electrodes. This can be achieved using laser annealing techniques with appropriate energy densities and the oxide layers that promote the growth of dense Ag layers.

**Acknowledgements** The author extends gratitude to Dr. Wen-Tse Hsiao from the Instrument Technology Research Center, National

Applied Research Laboratories, Hsinchu 30076, Taiwan, for their assistance in laser annealing and TEM investigation. The authors also acknowledge the financial support provided by the National Science and Technology Council of Taiwan R.O.C., under grant numbers (NSTC 111-2221-E-218-015 and 112-2221-E-218-005).

## Declarations

**Conflict of interest** The authors declare that they have no conflict of interest.

## References

- H.-N. Cui, S.-Q. Xi, *Thin Solid Films* **288**, 325–329 (1996)
- Y.-H. Tak, K.-B. Kim, H.-G. Park, K.-H. Lee, J.-R. Lee, *Thin Solid Films* **411**, 12–16 (2002)
- X. Yan, F.W. Mont, D.J. Poxson, M.F. Schubert, J.K. Kim, J. Cho, E.F. Schubert, *Jpn. J. Appl. Phys.* **48**, 120203 (2009)
- U. Betz, M.K. Olsson, J. Marthy, M.F. Escolá, F. Atamny, *Surf. Coat. Technol.* **130**, 361–368 (2019)
- X. Zhou, J. Xu, L. Yang, G. Zhu, Z. Yu, *J. Mater. Sci. Mater. Electron.* **26**, 6954–6960 (2015)
- S.J. Lee, S.H. Lee, H.W. Kang, S. Nahm, B.H. Kim, H. Kim, S.H. Han, *Chem. Eng. J.* **416**, 129028 (2021)
- F. Djéffal, H. Ferhati, A. Benhaya, A. Bendjerad, *Superlattices Microstruct.* **130**, 5751–5759 (2019)
- N.-F. Ren, L.-J. Huang, M. Zhou, B.-J. Li, *Ceram. Int.* **40**, 8693–8699 (2014)
- F. Li, Y. Zhang, C. Wu, Z. Lin, B. Zhang, T. Guo, *Vacuum* **86**, 1895–1897 (2012)
- H. Ferhati, F. Djéffal, A. Benhaya, *Superlattices Microstruct.* **129**, 176–184 (2019)
- Y. Djaoued, V.H. Phong, S. Badilescu, P.V. Ashrit, F.E. Girouard, V.-V. Truong, *Thin Solid Films* **293**, 108–112 (1997)
- G.S. Belo, B.J.P. da Silva, E.A. de Vasconcelos, W.M. de Azevedo, E.F. da Silva Jr, *Appl. Surf. Sci.* **255**, 755–757 (2008)
- J. George, C.S. Menon, *Surf. Coat. Technol.* **132**, 45–48 (2000)
- E. Benamar, M. Rami, C. Messaoudi, D. Sayah, A. Ennaoui, *Sol. Energy Mater. Sol. Cells* **56**, 125–139 (1999)
- J.H. Kim, K.A. Jeon, G.H. Kim, S.Y. Lee, *Appl. Surf. Sci.* **252**, 4834–4837 (2006)
- T. Maruyama, K. Fukui, *J. Appl. Phys.* **70**, 3848 (1991)
- Y.S. Jung, D.W. Lee, D.Y. Jeon, *Appl. Surf. Sci.* **221**, 136–142 (2004)
- K. Sreenivas, T.S. Rao, A. Mansingh, *J. Appl. Phys.* **57**, 384 (1985)
- E. Bertran, C. Corbella, M. Vives, A. Pinyol, C. Person, I. Porqueras, *Solid State Ion.* **165**, 139–148 (2003)
- W. Yang, Z. Liu, D.-L. Peng, F. Zhang, H. Huang, Y. Xie, Z. Wu, *Appl. Surf. Sci.* **255**, 5669–5673 (2009)
- M. Girtan, *Sol. Energy Mater. Sol. Cells* **100**, 153–161 (2012)
- P. Lei, X. Chen, Y. Yan, X. Zhang, C. Hao, J. Peng, J. Ji, Y. Zhong, *J. Electron. Mater.* **51**, 2645–2651 (2022)
- C. Guillén, J. Herrero, *Opt. Commun.* **282**, 574–578 (2009)
- K.-M. Lin, R.-L. Lin, W.-T. Hsiao, Y.-C. Kang, C.-Y. Chou, Y.-Z. Wang, *J. Mater. Sci. Mater. Electron.* **28**, 12363–12371 (2017)
- M. Rajendran, C.-E. Huang, K.-M. Lin, *Mod. Phys. Lett. B* **36**, 2242009 (2022)
- C.H. Hong, Y.J. Jo, H.A. Kim, I.-H. Lee, J.S. Kwak, *Thin Solid Films* **519**, 6829–6833 (2011)
- C. Guillén, J. Herrero, *Sol. Energy Mater. Sol. Cells* **92**, 938–941 (2008)
- L.L. Yang, D. Ge, H. Wei, F. He, X.D. He, *Appl. Surf. Sci.* **255**, 8197–8201 (2009)
- K.-M. Lin, S. Shinde, *J. Mater. Sci. Mater. Electron.* **32**, 5690–5697 (2021)
- Y.S. Kim, J.H. Park, D.H. Choi, H.S. Jang, J.H. Lee, H.J. Park, J.I. Choi, D.H. Ju, J.Y. Lee, D. Kim, *Appl. Surf. Sci.* **254**, 1524–1527 (2007)
- J.C. Kim, C.H. Shin, C.W. Jeong, Y.J. Kwon, J.H. Park, D. Kim, *Nucl. Instrum. Methods Phys. Res. B* **268**, 131–134 (2010)
- K.H. Choi, J.Y. Kim, Y.S. Lee, H.J. Kim, *Thin Solid Films* **341**, 152–155 (1999)
- S. Arai, T. Kikuhara, M. Shimizu, M. Horita, *Mater. Lett.* **303**, 130504 (2021)
- J.H. Kim, T.-W. Kang, S.-N. Kwon, S.-I. Na, Y.-Z. Yoo, H.-S. Im, T.-Y. Seong, *J. Electron. Mater.* **46**, 306–311 (2017)
- B.-J. Li, M. Zhou, M. Ma, W. Zhang, W.-Y. Tang, *Appl. Surf. Sci.* **265**, 637–641 (2013)
- Q. Xu, R.D. Hong, H.L. Huang, Z.F. Zhang, M.K. Zhang, X.P. Chen, Z.H.Y. Wu, *Opt. Laser Technol.* **45**, 513–517 (2013)
- H. Pan, D. Lee, S.H. Ko, C.P. Grigoropoulos, H.K. Park, T. Hoult, *Appl. Phys. A* **104**, 29–38 (2011)
- M.-F. Chen, K.-M. Lin, Y.-S. Ho, *Opt. Lasers Eng.* **50**, 491–495 (2012)
- N.-F. Ren, W.-Z. Wang, B.-J. Li, L.-J. Huang, Y. Zhang, *J. Mater. Sci. Mater. Electron.* **32**, 10644–10661 (2021)
- H.J. Kim, M.-J. Maeng, J.H. Park, M.G. Kang, C.Y. Kang, Y. Park, Y.J. Chang, *Curr. Appl. Phys.* **19**, 168–173 (2019)
- W. Chung, M.O. Thompson, P. Wickboldt, D. Toet, P.G. Carey, *Thin Solid Films* **460**, 291–294 (2004)
- C.-F. Ding, W.-T. Hsiao, H.-T. Young, *Ceram. Int.* **45**, 16387–16398 (2019)
- G. Jo, J.-H. Ji, K. Masao, J.-G. Ha, S.-K. Lee, J.-H. Koh, *Ceram. Int.* **44**, S211–S215 (2018)
- M. Rajendran, K.-M. Lin, W.-T. Hsiao, *Mod. Phys. Lett. B* **37**, 2340036 (2023)
- H.J. Cho, S.U. Lee, B. Hong, Y.D. Shin, J.Y. Ju, H.D. Kim, M. Park, W.S. Choi, *Thin Solid Films* **518**, 2941–2944 (2010)
- M. Li, Y. Wang, Y. Wang, X. Wei, *Ceram. Int.* **43**, 15442–15446 (2017)
- B. Barman, S.K. Swami, V. Dutta, *Mater. Sci. Semicond. Process.* **129**, 105801 (2021)
- G. Haacke, *J. Appl. Phys.* **47**, 4086 (1976)
- M. Mohamedi, F. Challali, T. Touam, M. Konstantakopoulou, V. Bockelée, D. Mendil, S. Ouhenia, D. Djouadi, A. Chelouche, *Appl. Phys. A* **129**, 545 (2023)

**Publisher's Note** Springer Nature remains neutral with regard to jurisdictional claims in published maps and institutional affiliations.

Springer Nature or its licensor (e.g. a society or other partner) holds exclusive rights to this article under a publishing agreement with the author(s) or other rightsholder(s); author self-archiving of the accepted manuscript version of this article is solely governed by the terms of such publishing agreement and applicable law.